Peer-Reviewed Technical Communication

Underwater Acoustic Network Simulation With Lookup Tables From Physical-Layer Replay

Roald Otnes, *Senior Member, IEEE*, Paul A. van Walree, *Member, IEEE*, Helge Buen, and Heechun Song

***Abstract*—An underwater acoustic network simulation methodology is presented that is based on lookup tables (LUTs) with physical-layer error ratios. These LUTs are prepared with a validated replay channel simulator, which is here driven by channel measurements from the Kauai Acomms MURI 2011 (KAM11) experiment. Three physical-layer candidates are considered: a coherent single-carrier scheme, a coherent multicarrier scheme, and an incoherent scheme. The three modulation schemes are operated at a fixed message size and at four different data rates. Low rates are more robust to noise, interference, and channel dispersion, but also more prone to collisions in a network with busy traffic, because the packets are longer. Error statistics for colliding packets have been measured and are incorporated in the network simulator as collision LUTs. Example simulations are presented for a reduced flooding protocol with or without retransmissions. The results demonstrate how retransmissions pose a tradeoff between performance at high and low traffic load. The best network performance is obtained if the highest data rate is selected that yields a reasonably well-connected network. Collision avoidance is more important than the extended connectivity offered by low-rate signaling. On the other hand, at a given bit rate, a physical-layer scheme with extended connectivity but relatively weak links is shown to outperform a scheme with stronger links over fewer connections.**

***Index Terms*—Channel models, communication channels, communication networks, computer simulation, lookup table, routing protocols, underwater acoustics, underwater communication.**

I. Introduction

THERE has been an increasing interest in underwater communication networks research. Owing to the cost and complexity of sea trials or test beds, much of this work is based on simulations. In network simulations, the physical layer is often modeled with empirical equations for noise and propagation loss [1], [2], as illustrated in Fig. 1(a). The resulting signal-to-noise ratio (SNR) for a given source level and range is transformed into bit error ratio (BER) and packet error ratio (PER) using text book formulas. Some recent examples of studies that have used such an approach are [3]–[5].

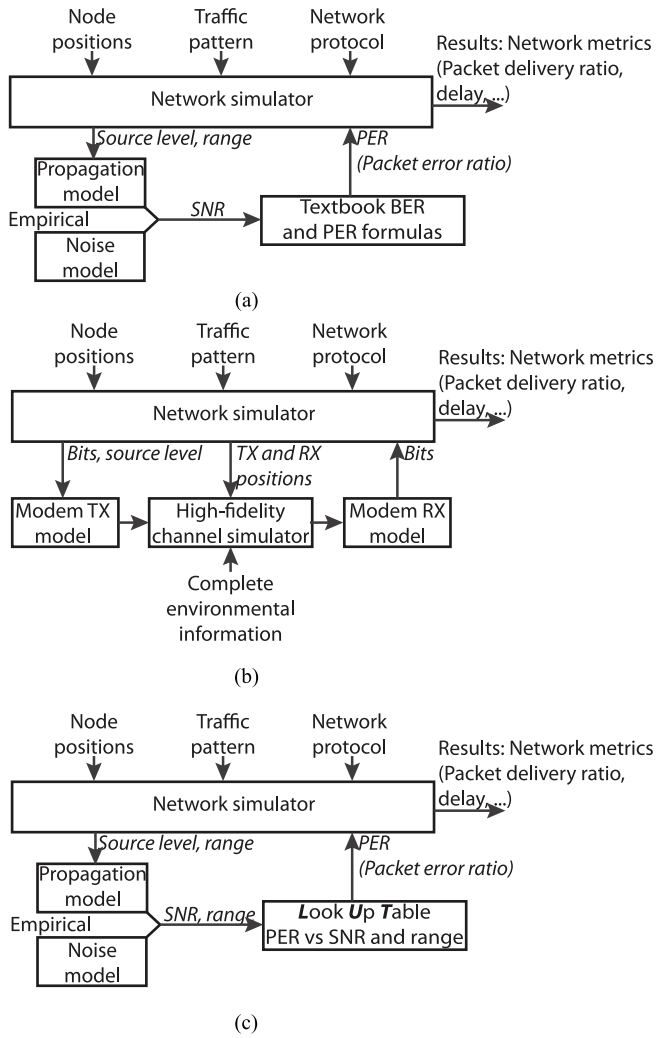

Fig. 1. Approaches to physical-layer modeling in network simulations. (a) Typical approach. (b) Ideal approach. (c) Lookup table approach.

While useful for comparing network protocols in a design stage, propagation loss and noise models only yield estimates of the SNR at the modem receiver. The assumption that modem performance can be predicted from SNR alone is not met in many practical settings. Unless one operates at low SNR, the maximum achievable data rate is typically limited by delay-Doppler spreading [6].

To increase the realism, one could in principle invoke from the network simulator, each time a transmission is made, a detailed model of the physical layer (acoustic communication

Manuscript received February 08, 2015; revised June 05, 2015; accepted August 19, 2015. Date of publication September 23, 2015; date of current version October 09, 2015. This paper was presented in part at the Underwater Communications and Networking (UComms) Conference, Sestri Levante, Italy, Sep. 2014.

Associate Editor: J. Potter.

R. Otnes, P. A. van Walree, and H. Buen are with the Maritime Systems Division, Norwegian Defence Research Establishment (FFI), Horten NO-3191, Norway (e-mail: roald.otnes@ffi.no).

H. Song is with the Scripps Institution of Oceanography, University of California San Diego, La Jolla, CA 92093-0238 USA.

Digital Object Identifier 10.1109/JOE.2015.2471736

TABLE I
DSSS AND FRSS PARAMETERS

R	K	Symbol rate (s^{-1})	Taps DSSS	Taps FRSS
1	1	2800	75	75
2	3	933	75	3×25
3	7	400	75	7×11
4	15	187	75	15×5

channel and modem). Unfortunately, this scenario, shown in Fig. 1(b), is impractical because physical-layer simulations are much more time consuming than network simulations. Further, there are no standardized channel models, and only a few validated channel models (see [7, Table I] and [8]).

The variation in acoustic channels is enormous [9], [10], and it can be challenging to capture all effects of the environment on communication performance in a model-based channel simulator [11]. Modeling time variations in the channel is a particular challenge, since this requires knowledge of, among other things, surface gravity waves [12] and internal waves [13], and how sound interacts with them, and the effects of platform motion [10]. Another complication is that sophisticated acoustic models require detailed environmental information, which may be difficult to obtain.

Recent channel simulation efforts providing more than SNR include acoustic modeling [14], [15], stochastic modeling [16], and channel replay [17]–[19]. A replay simulator relies on measurements of the time-varying impulse response in the environment of interest, but once such data are available, the physical layer can be simulated with high fidelity [7]. This paper proposes to adopt a channel replay physical-layer model for network simulations. The complexity issue is dealt with by precomputing PERs for various link distances, signal types, data rates, etc., and storing these in lookup tables (LUTs) which the network simulator invokes as required. This approach is illustrated in Fig. 1(c).

To our knowledge, apart from this paper's precursors [20], [21], physical-layer modeling at this level of realism has not previously been integrated into network simulations. Parrish *et al.* [15] and the World Ocean Simulation System (WOSS) [22], [23] use a ray tracer and available environmental information to estimate propagation losses for network simulations, but do not consider the effect of delay and Doppler spread on physical-layer performance, except for considering signal energy received outside a certain delay spread as noise. Other approaches apply direct or stochastic replay of actual packet error or bit error sequences observed in experiments [24]–[26], but cannot be used to predict the performance of other physical-layer methods than those used in the experiment.

Another contribution of this paper is to present in some detail all steps involved in applying the proposed approach: from obtaining suitable channel measurements, assessing the performance of different physical-layer methods by channel replay simulations, building and examining the LUTs, understanding the network topologies resulting from application of the LUTs to a given network layout, to presenting and interpreting network simulation results for the scenario and network protocol under study. Along the way, interesting observations are made with respect to physical-layer performance as well as network protocol performance.

The outline of the paper is as follows. A short overall description of the proposed LUT approach is given in Section II. The physical layers under consideration are presented in detail in Section III, and the Kauai Acomms MURI 2011 (KAM11) channel measurements used in the study are introduced in Section IV. Section V describes the channel simulator and investigates the performance of the physical-layer schemes in the KAM11 channels, which is made available to the network simulator in the form of LUTs. The network protocol under study, "Dflood," is described in Section VI, and Section VII explains how the LUTs are used in the network simulations. The network simulation setup is described in Section VIII, and simulation results presented and discussed in Section IX. Finally, conclusions are drawn in Section X.

II. OVERALL APPROACH

In the European Defence Agency (EDA) project Robust Acoustic Communications in Underwater Networks (RACUN) [27], an underwater acoustic communication network simulation method was developed which incorporates LUTs from replay-based physical-layer simulations [20]. In this paper, we present a case study to demonstrate the application of this method to an environment and physical-layer methods outside the RACUN project.

Fig. 2 gives an overview of the approach. The LUT introduced in Fig. 1(c) is precomputed through physical-layer simulations, by performing the following procedure a number of times: A packet of bits is encoded and modulated by a model of the modem transmitter; the modulated signal is passed through a replay channel and complemented by noise; and the resulting channel output is detected, demodulated, and decoded by a model of the modem receiver. The decoded bits are compared with the transmitted bits to check whether the packet is in error (i.e., has one or more bit errors). It is assumed that the physical layer (modem) includes forward error correction as well as a cyclic redundancy check (CRC) code for error detection. A number of independent packets can be passed through a given channel, permitting estimation of the PER as the fraction of packets in error. This can be done for channels measured over different ranges and at different SNR values.

The SNR in the network simulations is computed from empirical models for propagation loss and noise. These models can be tuned to *in situ* measurements of propagation loss and noise. When the channel impulse response, propagation loss, and noise characteristics are all matched to measured data from the same experiment, the ingredients are present for highly realistic network simulations.

III. THE PHYSICAL LAYERS

The network simulations are performed with three different modulation schemes. These schemes are tested at various data rates, indicated by the rate parameter $R \in \{1, 2, 3, 4\}$, whose

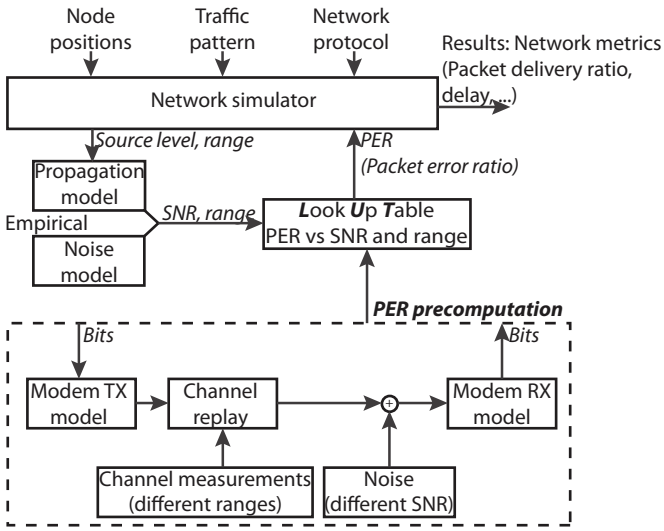

Fig. 2. Proposed LUT-based approach to physical-layer modeling in network simulations.

role is just to group signals of different schemes which have approximately the same data rate. $R = 1$ is the highest rate and $R = 4$ is the lowest rate. The schemes are direct-sequence spread spectrum (DSSS), frequency-repetition spread spectrum (FRSS), and M-ary frequency-shift keying (MFSK). DSSS is a single-carrier coherent scheme, FRSS is a multicarrier coherent scheme and a form of frequency-division multiplexing, and MFSK is an incoherent scheme. The notation DSSS1 will be used to denote DSSS transmitted at rate $R = 1$, etc. The computer code of all schemes has been optimized for speed, and FRSS and MFSK have actually been implemented in experimental modems. One should keep in mind, while examining the performances, that low-complexity implementations are considered. The remainder of this section gives a brief description of the schemes, starting with the parts that they have in common, and continuing with details of the parts that differ. Note that some signal parameters were changed after the study described in [28].

A. Common Parts

All signals, regardless of modulation type and rate, are equipped with a single-carrier m-sequence detection preamble. The sequence length is $2^{6+R} - 1$ for $R \in \{1, 2, 3, 4\}$, the chip rate is 2800 chips/s, and the pulse shape is root raised cosine with rolloff factor $\beta = 1/3$. The detector Doppler bank covers the TX/RX radial velocity interval from -2 to $+2$ m/s, which is sufficient for the KAM11 tow speeds. The peak filter output across all Doppler channels is compared with a threshold value, and in case of detection, the communication receiver is informed about the start sample of the signal in the raw data, and the value of the Doppler shift estimate. The receivers of all schemes remove the estimated nominal Doppler shift by resampling. Note that the preamble length increases with a decreasing data rate, permitting detection at lower SNR and providing a more accurate Doppler estimate. Detection thresholds are set to yield one false alarm per day in the colored noise described in Section V-B.

All schemes further use rate-1/2 convolutional channel coding with constraint length 9, and soft-decision Viterbi decoding. User bits are put through a random interleaver after the convolutional encoding, and are deinterleaved before the Viterbi decoder. Bit errors occurring in clusters are spread out in this manner, providing the Viterbi decoder with better opportunities to correctly decode the message.

With preamble detection and channel coding being identical, explanations for performance differences between schemes can be narrowed down to the raw modulation format and implementation choices therein.

B. Coherent Schemes

1) DSSS: DSSS is modulated onto a single carrier with a quadrature phase-shift keyed (QPSK) symbol constellation, using maximal-length spreading codes with length $K = 2^R - 1$. The chips are root-raised-cosine pulses $p(t)$ with $\beta = 1/3$, transmitted at a rate of $K/T = 2800$ chips/s, where T is the symbol duration. This is the same pulse that is used for the preamble. Initial training symbols are prepended, and periodic training symbols are interleaved with the information carrying symbols. If the complex symbol value is denoted by $z(n) \in \{(1+i)/\sqrt{2}, (-1+i)/\sqrt{2}, (-1-i)/\sqrt{2}, (1-i)/\sqrt{2}\}$, the spreading code by $c(k) \in \{-1, 1\}$, the pulse shape by $p(t)$, and the carrier frequency by ω_c, the transmitted waveform is given by the real part of

$$s_D(t) = \sum_{n=1}^{N} \sum_{k=1}^{K} z(n)c(k) \times p\left(t - \frac{k-1}{K}T - nT\right) \exp\left(i\omega_c t\right). \quad (1)$$

Fig. 3 sketches the modulation format.

The receiver is implemented with a chip-rate hypothesis equalizer, where chip decisions are taken in retrospect after symbol despreading [29]. A linear equalizer is implemented with the plain least mean squares (LMS) tap update algorithm, and an integrated phase-locked loop (PLL) to deal with residual Doppler shifts [30]. Fig. 4 sketches the receiver block diagram. When the symbol is a training symbol, the reference chip is always correct. Information symbols are equalized four times, using as reference chips the spreading code multiplied by the four possible phases of a QPSK symbol. Each of the four equalization hypotheses starts with the filter coefficients and phase estimate θ stored at the end of the previous symbol. A decision device is applied after despreading the equalized chips for each of the four hypotheses. The dotted line down from the decision device indicates that the equalizer state corresponding to the most probable hypothesis is kept as the starting point for the next symbol, and the dotted line up indicates that only the symbol corresponding to that hypothesis is sent further down the chain.

2) FRSS: FRSS is a simplified version of the multicarrier scheme described in [31], and shares many signal parameters with DSSS. The key difference is that DSSS subdivides the symbols in time, and FRSS in frequency, using K sub-bands where

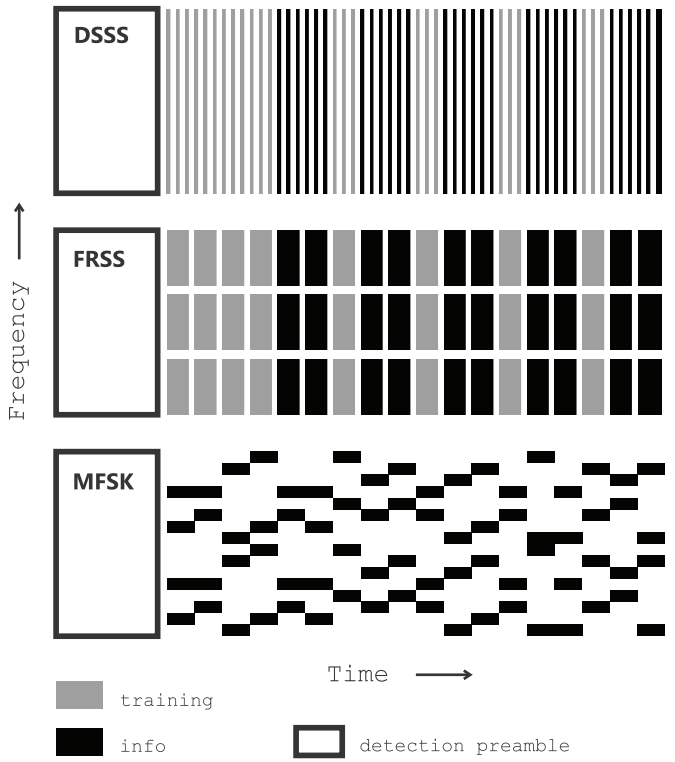

Fig. 3. Modulation formats illustrated for $R = 2$. Following the initial training, every third symbol is a periodic training symbol for DSSS and FRSS. MFSK2 has redundancy in the frequency domain by carrying the same data in the lower and upper halves of the band. Note that the figure is very schematic and not to scale.

DSSS uses K chips. A sketch of the modulation format is included in Fig. 3. The transmit signal is given by the real part of

$$s_{\mathrm{F}}(t) = \left(\sum_{n=1}^{N} z(n)p(t/K - nT)\right)\left(\sum_{k=1}^{K} c(k)\exp(\mathrm{i}\omega_k t)\right) \tag{2}$$

where ω_k is the angular carrier frequency of the kth frequency band. The carriers are offset from the overall center frequency ω_{c} and spaced by $(1+\beta)/T$ to obtain contiguous sub-bands

$$\omega_k = \omega_{\mathrm{c}} + 2\pi\left(k - \frac{K+1}{2}\right)\frac{1+\beta}{T}. \tag{3}$$

The spreading code $c(k)$ does not spread the spectrum, contrary to the DSSS case, but has the desirable property that it reduces the peak-to-average power ratio of the FRSS waveform. The total bandwidth is $B = (1+\beta)KT^{-1}$ for both waveforms.

The FRSS receiver diagram in Fig. 4 shows similarities and differences with DSSS. After the sub-bands are individually basebanded and bandpass filtered, K linear equalizers are applied with LMS tap updates. The multichannel equalizer performs joint equalization and despreading without knowledge of $c(k)$. The PLL is driven by the error signal after despreading, and yields a phase estimate θ characteristic of ω_{c}. However, the phase rotation applied to the sub-bands is multiplied by $\omega_k/\omega_{\mathrm{c}}$. This reflects the fact that Doppler frequency shifts are proportional to the passband frequency. (The resampling described in Section III-A may remove most of the Doppler, but the time-varying residual is still proportional to the frequency.)

3) DSSS and FRSS Parameters: FRSS tracks the channel at the symbol rate, using a tap spacing of $3T/4$, whereas DSSS tracks at the chip rate with a tap spacing of $3T/(4K)$. This spacing is sufficient for the selected rolloff factor $\beta = 1/3$ [32]. For all signals, an equalizer span of $\approx$20 ms is used. This gives the tap configurations listed in Table I. Note that FRSS is identical to DSSS for $R = K = 1$, which gives a nonspread single-carrier signal. The waveforms and receiver performances are the same. For larger K, FRSS employs K shorter equalizers, but the total number of filter taps $N_{\mathrm{taps}} \approx 75$ remains the same. The LMS step-size parameter is set at $\mu = 0.3/N_{\mathrm{taps}}$ for both schemes, and the soft input required for the Viterbi decoding uses the assumption of Gaussian symbol statistics at the output of the adaptive filters. The computation of the corresponding log-likelihood ratio (LLR) is detailed in [31].

There are several factors that give rise to performance differences between DSSS and FRSS for increasing K. DSSS has more frequent tap updates and can track faster channel fluctuations. FRSS has a wideband PLL, whereas the narrowband PLL of DSSS saddles the equalizer with residual phase distortion over the signal band. The DSSS receiver despreads after equalization, whereas FRSS performs a joint operation. An FRSS decision error gives a single incorrect tap update, while a DSSS decision error gives K consecutive update errors. The overall effect of these differences is difficult to predict, and may well depend on channel and noise conditions.

C. MFSK

The MFSK scheme is incoherent and uses discrete tones to encode the information. The modulation principle is 1-of-4 MFSK, which means that each symbol is a tone that takes one of four frequencies depending on two binary bits, mapped to a symbol $z(n) \in \{0,1,2,3\}$. Multiple 1-of-4 MFSK signals are transmitted simultaneously on different subcarriers.

Both the transmitter and the receiver utilize (inverse) fast Fourier transforms (FFTs) for generation and detection of the tones. Using $L = 128$ point FFTs and $M = 4$ bins per symbol makes room for $L/M = 32$ symbols (subcarriers) in each of the FFT frames, and the data packet consists of several such frames $u \in \{1,\ldots,U\}$ along the time axis, as illustrated in Fig. 3.

The above explained signal properties are common for all the MFSK rates R. The difference between the rates is how data redundancy is distributed over time and frequency in order to mitigate multipath delay spreading and the corresponding fades in the spectrum [33]. Table II shows how the robustness is divided between frequency redundancy (J) and tone duration (ζ).

The frequency redundancy is a form of spread spectrum whereby each pair of bits is repeated in J MFSK symbols, transmitted in J sub-bands of the signal. Each sub-band carries $Q = L/(JM)$ symbols, indexed by $q \in \{1,\ldots,Q\}$, and each symbol $z(n)$ carries two gray-encoded bits. The location of the nth symbol in terms of u and q follows from $n = (u-1)Q + q$.

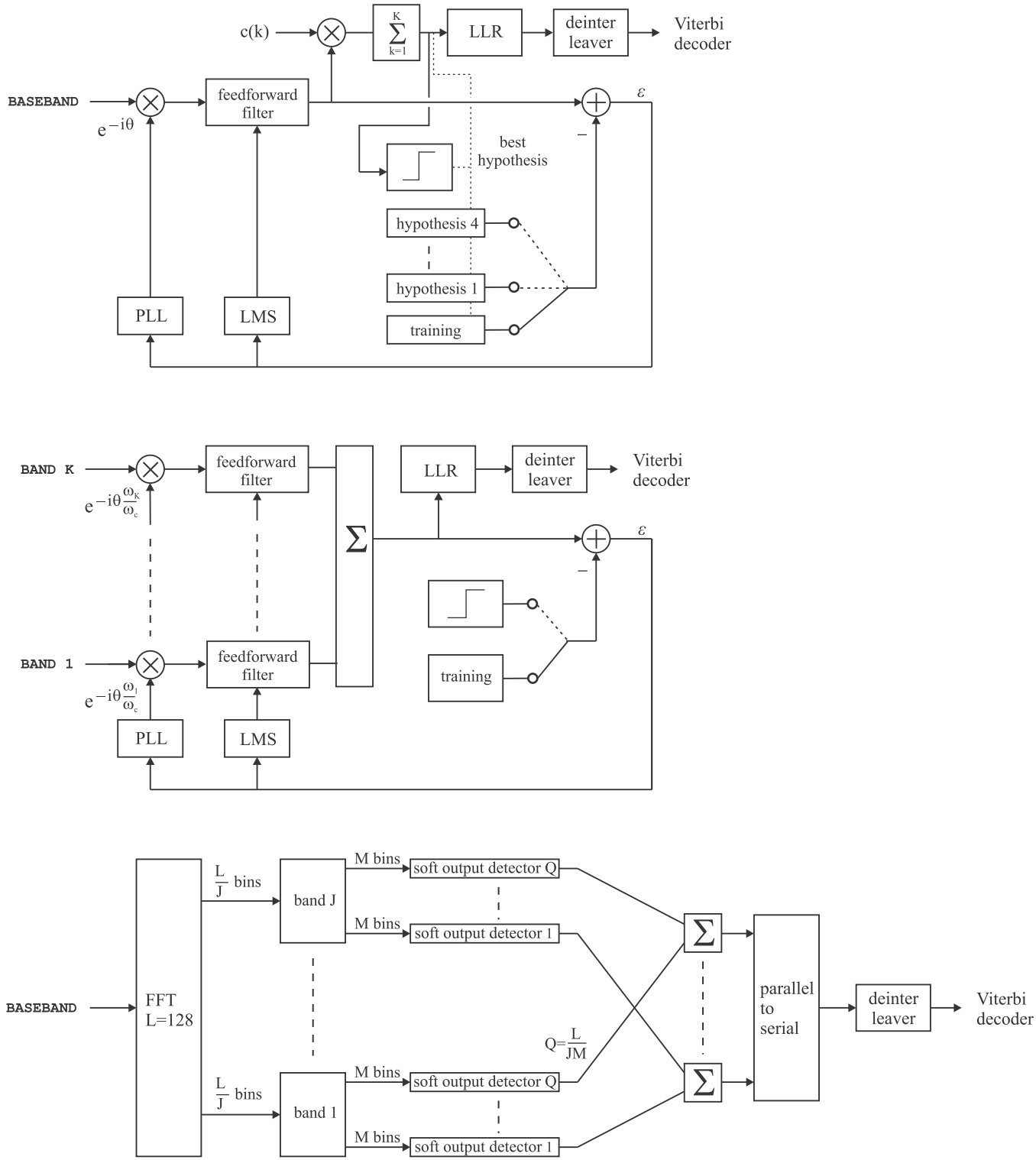

Fig. 4. Receiver block diagrams. From top to bottom: DSSS, FRSS, and MFSK.

The number of inverse fast Fourier transform (IFFT) frames is $U = \lceil N_\mathrm{b}/(2Q) \rceil$, with N_b the total number of transmitted bits, including coding. In the time domain, the waveform reads

$$s_\mathrm{M}(t) = \sum_{u=1}^{U} \sum_{j=1}^{J} \sum_{q=1}^{Q} r(t - u\zeta T) \exp(\mathrm{i}\omega_{u,j,q}\, t + \phi_{j,q}) \quad (4)$$

with

$$\omega_{u,j,q} = \omega_c - 2\pi B \left(\frac{1}{2} - \frac{[(j-1)Q + q - 1]\, M + z(u,q)}{L} \right) \quad (5)$$

where $\phi_{j,q}$ is a randomized phase offset, $r(t)$ is a rectangular pulse with length ζT, $T = L/B$, and $\zeta \in \{1, 2\}$ is a tone duration parameter, where $\zeta = 2$ means that a guard interval (cyclic

TABLE II
MFSK SIGNAL PARAMETERS

R	Frequency redundancy J	Tone duration parameter ζ
1	1	1
2	2	1
3	2	2
4	4	2

prefix) equal to T is used; see below. We use a bandwidth of $B = 3600$ Hz, which gives $T = 35.6$ ms.

Demodulation is performed with FFTs, as shown in Fig. 4. Soft output is calculated for each symbol separately before frequency redundancy combining and Viterbi decoding. Note that the FFT is an $L = 128$ point operation for all signal types. This implies that the full tone duration T is used for $R \in \{1, 2\}$. For $R \in \{3, 4\}$ (i.e., $\zeta = 2$), the first half of the tones is not used and acts as a guard interval (cyclic prefix). It reduces reverberation from the previous symbol into the second half of the tone, whereas reverberation from the first half into the second half adds energy at the correct frequency. The longer tone duration also relaxes the synchronization requirement for the FFT.

D. Packet Size, Rates, and Complexity

All signals are generated with a fixed physical-layer service data unit (PSDU) size of 256 b.[1] Signal parameters such as K and the training overhead of the coherent schemes, and the MFSK parameters of Table II, then result in the effective bit rates of Table III. At each value of R, the three schemes have approximately the same effective rate, and for each increment of R, the effective rate is approximately halved. The effective bit rate is computed as the PSDU size divided by the total signal duration, including all overhead. The overhead of the detection preamble and initial training (in case of xxSS) is considerable at such small packet sizes. The table illustrates this by listing also the raw data rates, which are the effective rates in the limit of an infinite PSDU size. In fact, this is the main reason why the higher rates are equipped with shorter preambles, as mentioned in Section III-A. For instance, $R = 1$ would be very inefficient with a 1023-chip preamble.

Keywords describing the physical-layer modem algorithms are single-hydrophone reception, fixed receiver parameters, and low complexity. Table IV shows demodulation times measured in Matlab® on a 64-b workstation with Intel® i7-3820 CPU. MFSK has the lowest complexity and needs about 20 ms to decode a single packet. FRSS is also fast and demonstrates that a multichannel equalizer is not necessarily complex. DSSS has the highest complexity, but demodulation times are still short compared to the signal duration. DSSS1 has a longer computation time than FRSS1, although its waveforms and error ratios

[1]The PSDU size is the number of bits from the layer above expedited by the physical layer in each transmission. In a military context, 256 b including network protocol overhead can be a typical size of a short contact report.

TABLE III
PREAMBLE LENGTH, TOTAL SIGNAL DURATION, AND DATA RATES. XXSS STANDS FOR BOTH DSSS AND FRSS

R	Preamble (chips)	Signal length (s)		Eff. rate (bit/s)		Raw rate (bit/s)	
		xxSS	MFSK	xxSS	MFSK	xxSS	MFSK
1	127	0.40	0.41	642	627	1867	900
2	255	0.76	0.74	336	347	622	450
3	511	1.47	1.43	174	178	267	225
4	1023	2.82	2.75	91	93	124	113

TABLE IV
RECEIVER COMPLEXITY

R	Demodulation time (s)		
	DSSS	FRSS	MFSK
1	0.072	0.043	0.019
2	0.10	0.035	0.018
3	0.16	0.043	0.018
4	0.27	0.069	0.023

are precisely the same. The reason is that DSSS uses hypothesis equalization, which (in case of QPSK) implies that each information symbol is equalized four times.

IV. KAM11 CHANNEL MEASUREMENTS

Impulse responses were obtained with a correlative channel sounder during the KAM11 experiment. This experiment was conducted in shallow water (80–200 m deep) off the western side of Kauai, HI, USA, over the period June 23–July 12, 2011 [34], [35]. The objective of KAM11 was to obtain acoustic and environmental data appropriate for studying the coupling of oceanography, acoustics, and underwater communications. Both fixed and towed source transmissions were carried out to multiple receiving arrays at different distances. In this paper, we utilize the data set collected during a towed-source run on July 8 (JD189) in the band of 4–8 kHz during a three-hour period (16:00–19:00 Z) in about 100-m-deep water. The water column in the KAM11 environment was variable with a mixed layer depth of 40–60 m and downward-refracting below, while the geoacoustic property of the seafloor was typical of sand [36].

The data set consists of soundings over 16 distances from 0.5 to 8.6 km. At each distance, a continuous train of 256 linear chirps was transmitted by the towed source, and recorded on a 16-element vertical array. The frequency band is 4–8 kHz, the chirp duration $T = 128$ ms, and the probe signal duration $256 \times T = 32.8$ s. Channel estimates are obtained by removing the nominal Doppler shift by resampling, correlating the recorded chirp train with the transmit chirp, and stacking the resulting impulse response snapshots.

Channel characteristics are illustrated by Fig. 5, which shows the power delay profile and the wideband Doppler power spectrum at two distances. There is a series of discrete arrival clusters at close range, which degenerate into a weaker, continuous

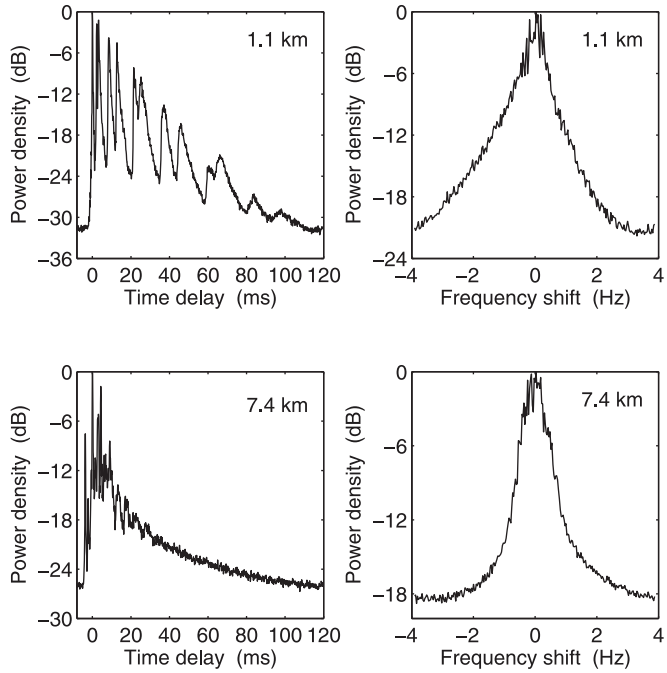

Fig. 5. Normalized delay profile and Doppler spectrum for hydrophone # 8 at signaling distances of 1.1 and 7.4 km. The computation method is detailed in [10].

reverberation tail as the range increases. The cause is attenuation of reflected paths by boundary losses. The longer the range, the larger is the number of boundary interactions of steep rays and the stronger is their attenuation. This also explains the narrowing of the Doppler spectrum with range. Rays with a large number of surface interactions contribute most to the tails of the Doppler spectrum. Note that the Doppler spread also has a significant contribution from time-varying motion of the towed source, which in principle is independent of range and delay.

V. Channel Simulation

A. Channel Replay

The physical-layer simulations couple a software implementation of modem transceiver algorithms to an acoustic channel simulator. Direct replay of measured impulse responses is used to mimic the acoustic channel [7], [17]. This simulation method faithfully mimics the ocean in the sense that it replays the time-varying impulse response exactly as measured at sea. Delay spread and Doppler spread are naturally included, as well as frequency-dependent path loss and time-varying path delays, which are important for wideband signaling. Stationary and nonstationary channels can be replayed, and nominal Doppler shifts that were removed in the probe signal processing are reinserted.

This technique has been validated for several areas and modulation schemes, with error ratios in simulation close to the corresponding error ratios at sea [7]. Simulation errors are predominantly due to measurement errors of the employed channel sounder, and can be minimized by discarding channels with obvious estimation errors. Common reasons for rejection are an insufficient SNR of the recorded probe signal, aliasing in delay, and aliasing in Doppler [37]. A quality check on the KAM11 data set led to the exclusion of hydrophone channels with insufficient SNR at the longer ranges. The 1.1-km data in Fig. 5 show that aliasing in delay is below 30 dB, and aliasing in Doppler is below 20 dB of the maximum. At longer ranges, the delay and Doppler spreads decrease, due to the attenuation of surface- and bottom-reflected paths.

The communication packets of Section III were propagated through the archive of KAM11 channels, where the availability of a receiver array permits simulation of many independent packets with direct replay. This can be explained by considering a channel probe signal of length 32 s and, as an example, a 1-s packet. The maximum number of packets that fit into the 32-s channel replay, without overlap, is about 28, allowing also for appropriate pauses between successive packets to avoid reverberation of one packet leaking into the next one. Many more independent realizations are possible by propagating 28 packets through the channels measured on the 16 available hydrophones, assuming (partly) uncorrelated channels. This results in $28 \times 16 = 448$ packets. The simulations in the remainder of this paper use 100 packets at each transmission range, systematically drawn from the 448 available packets.[2] Reported error ratios are thus depth averages over the array.

B. Link-Layer Simulations

Link-layer simulations are performed in ideal (dispersionless) channels and in the KAM11 acoustic channels, with additive white Gaussian noise (AWGN) and additive colored Gaussian noise (ACGN). The ACGN falls off with 6 dB over the signal bandwidth from 4 to 8 kHz, which is in agreement with noise spectra measured during KAM11 [35].

A packet propagated through a replay channel has an arbitrary (uncalibrated) level, and the desired SNR is achieved by scaling the added noise. The noisy packets are fed to the receivers for decoding, resulting in LUTs for the network simulations with PER as a function of range, SNR, and signal type. As mentioned before, the PER is a depth average value.

The link-layer performance charts of Section V-C are based on range-averaged versions of these LUTs. To be precise, every point on the curves presented in Section V-C is an average over 16 (ranges) $\times$ 100 (realizations) $=$ 1600 packets. Different points on the same curve use the same 1600 packets, but different amounts of added noise. Results for the dispersionless AWGN channel use a single packet with 1600 noise realizations.

C. Link-Layer Performance

This section examines the performance of the modulation schemes in the absence of a network scenario. As an initial receiver check, the PER is plotted in Fig. 6 versus E_b/N_0 in the ideal AWGN channel, where E_b is the energy per bit, taking all overhead into account, and N_0 is the noise power spectral density (PSD). The curves are very similar in shape, but there are differences up to 6 dB between modulations and rates. There are more reasons than just the difference in theoretical BER between FSK and phase-shift keying [38]. First, it is stressed that the curves in Fig. 6 are not theoretical, but obtained with actual

[2]Note that the total of 448 is for the example of a 1-s packet. The actual number depends on the actual packet length.

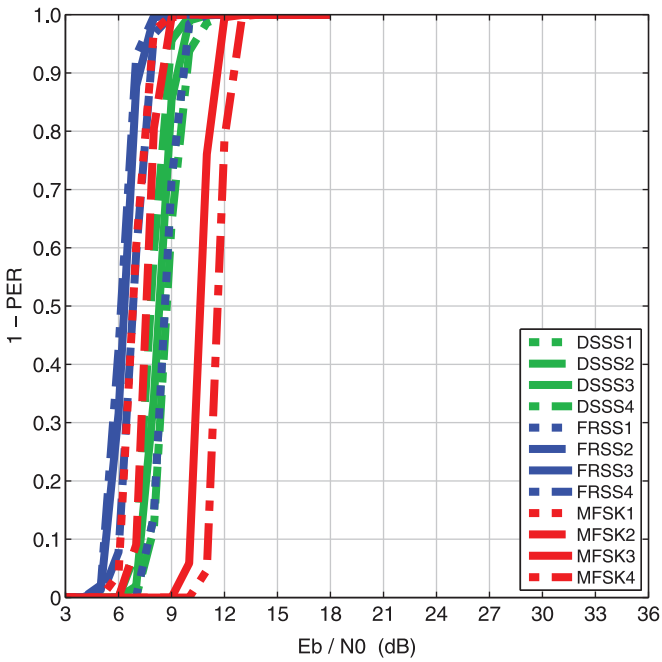

Fig. 6. PER versus E_b/N_0 in the ideal AWGN channel. The curves of DSSS1 and FRSS1 are overlapping.

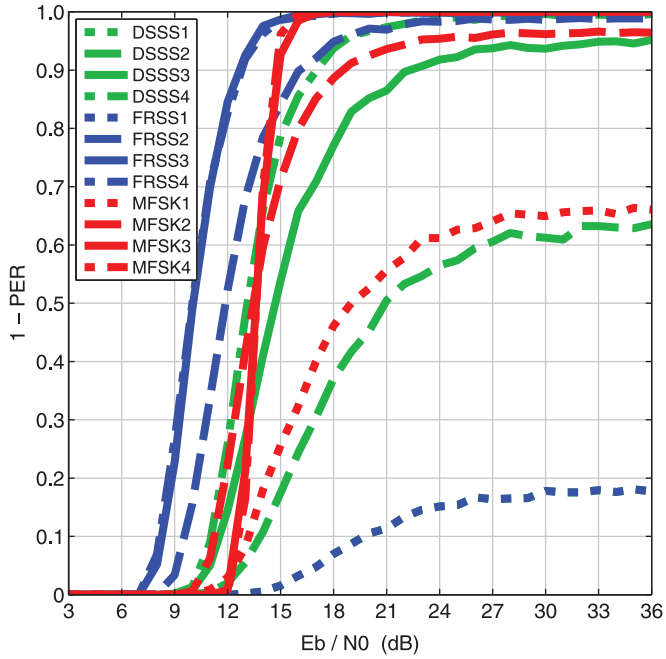

Fig. 7. PER versus E_b/N_0 in AWGN averaged over the KAM11 channels. The curves of DSSS1 and FRSS1 are overlapping.

receivers with acoustic modem parameter settings. Differences arise because of different amounts of overhead and redundancy, and because practical modem settings are not the best choice for an ideal channel.

The DSSS equalizer has 75 taps, for instance, far more than required for a dispersionless channel, where its only tasks are fine synchronization and acting as a filter matched to the pulse shape. There are many taps where there is no signal, resulting in noise amplification. FRSS, on the other hand, has short equalizers for large K and operates more stably at low SNR.

The worst performers in the ideal AWGN channel are MFSK3 and MFSK4, and for a simple reason. These two signals use a guard interval containing signal energy that is disregarded by the receiver. Half of the signal energy is wasted, which results in a 3-dB shift to the right.

Fig. 7 shows what happens when the dispersionless channel is replaced by acoustic channels. More precisely, the shown curves represent the PER averaged over the KAM11 channels. Achieving the same PER as in Fig. 6 requires a higher SNR for all signals, and some signals no longer reach zero PER, no matter how high the SNR. The reason is that modem performance is generally limited by noise plus interference. Multipath propagation and Doppler can only be handled to a certain degree, and the remaining signal power acts as self-interference. A high SNR alone is no guarantee for a reliable link. Low-rate, spread-spectrum-type signals can tolerate more interference than high-rate signals, but, for the same PSDU size they are also longer and prone to collisions in a network with busy traffic.

MFSK1 outperforms DSSS1 and FRSS1, which may be because the latter schemes have a much higher raw rate (Table III). They are essentially high-rate systems with considerable training overhead, which MFSK does not need. FRSS is the best performer at the other rates, and all schemes reach zero

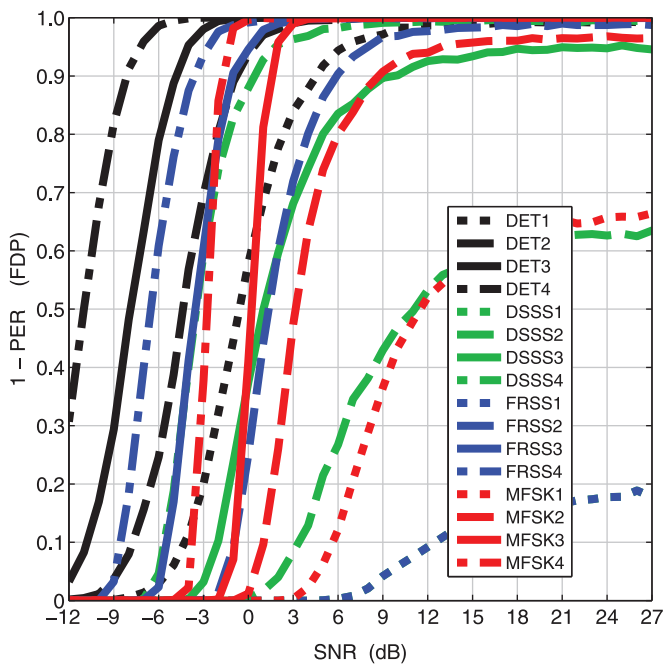

Fig. 8. PER and fraction of detected packets (FDP) versus SNR in ACGN, averaged over the KAM11 channels. The curves of DSSS1 and FRSS1 are overlapping.

PER if the rate is sufficiently reduced. Unlike the dispersionless case, the guard interval of MFSK3 and MFSK4 now pays off. MFSK2 still has the edge at low SNR, but MFSK3 and MFSK4 perform better at high SNR.

Note that the SNR required to achieve a given PER depends on the delay-Doppler spread function of the channel. Since the curves are averages over channels with different delay-Doppler spreads, they have a longer transition regime from high to low PER than the corresponding curves in Fig. 6. The exceptions are MFSK3 and MFSK4, whose curves are almost as steep. Their

Parameters defined by the rules: T_{min}, T_{max}, N_{Dupl}, T_{Dupl}, $N_{Retrans}$, $T_{Retrans}$.

Basic flooding rules:

- Each transmitted packet contains a hop counter, source and destination address, and a sequence number. A duplicate of a packet is recognized by having the same source and destination address and sequence number. The destination address may be a multicast address if the network addressing scheme allows.
- When a new packet is received from the application layer, send it down to the MAC layer immediately with hop counter set to 1.
- When a packet is forwarded, the hop counter is incremented by 1.
- First time a given packet from and to other nodes is encountered, schedule it for forwarding after a delay drawn uniformly from $[T_{min}, T_{max}]$.
- Duplicates received after relaying has been performed will be discarded.

Counter-based flooding reduction scheme:

- Duplicates received with a higher hop counter (than what is already stored for this packet) are counted, n_d being the number of duplicates received (not including the original packet or duplicates with the same or a lower hop counter).
- When a duplicate is received with a lower hop counter (having traveled fewer hops), the hop counter of the packet to be forwarded will be updated to the value of the hop counter of the received duplicate, plus one.
- Each time a duplicate with a higher hop counter is received, the node will draw a random number $r \in (0, 1]$. If the number of duplicates received $n_d > N_{Dupl} - r$, the forwarding is discarded. N_{Dupl} is a predefined maximum number of duplicates, which may be non-integer. This means that if $n_d = \lfloor N_{Dupl} \rfloor$, the forwarding is discarded with probability equal to the fractional part of N_{Dupl}, and if $n_d > \lfloor N_{Dupl} \rfloor$, the forwarding is always discarded.

Adaptive backoff:

- If forwarding is not canceled by the rule above, it is delayed by a time T_{Dupl} beyond the already scheduled forwarding time (adaptive backoff).

Last-hop acknowledgment to stop unnecessary forwardings:

- The end destination will immediately (with absolute precedence) broadcast (single hop) a "receive notification" message containing the original packet identifier. This can be received by all neighbours but shall never be forwarded.
- When a node receives a "receive notification" it will discard any forwarding of that packet.
- Last-hop acknowledgment is disabled for packets with multicast destination address.

Optional retransmissions:

- When a packet is first scheduled for forwarding, set a retransmission counter for that forwarding to $N_{Retrans}$. If $N_{Retrans} = 0$, retransmissions are disabled.
- Whenever a packet is forwarded, if the retransmission counter for that forwarding is larger than zero: Schedule a retransmission with an additional delay drawn uniformly from $[T_{Retrans}/2, T_{Retrans}]$, and decrement its retransmission counter.
- A scheduled retransmission is subject to the same rules to cancel or delay forwarding, as the first scheduled forwarding of a packet.
- Retransmissions are always disabled for "receive notification" packets.

Fig. 9. Dflood protocol rules.

guard interval renders them fairly insensitive to the channel characteristics, as illustrated in Section VII-B.

White noise is rarely seen in the oceans, and the network simulations therefore use LUTs computed with ACGN. The concept of E_b/N_0 does not apply to colored noise, but the computations of Figs. 6 and 7 were repeated with ACGN, and the conclusion is that the PER curves are virtually the same between ACGN and AWGN when the noise PSD at the signal center frequency equals N_0 (not shown).

Finally, Fig. 8 shows the PER curves versus the acoustic SNR instead of E_b/N_0. These are range averages of the LUTs used in the network simulations. As the bit rate decreases, all schemes can tolerate more interference and more noise. The latter observation implies longer communication ranges at a given source level.

In Figs. 6–8, a packet whose preamble is not detected counts as a packet error. The influence of missed detections on the PER curves is small, demonstrated by the fraction of detected packets, included as the black curves in Fig. 8.

VI. Network Protocol Under Study

We consider the "Dflood" reduced flooding protocol described in [20], [39], and [40]. Dflood is a flooding-based protocol where a "counter-based scheme" [41] for flooding

restriction is combined with a mechanism for adaptation of backoff times. Optionally, Dflood can also employ retransmissions, in which case scheduled retransmissions are subject to the same flooding restriction rules as the initial forwarding of a packet.

The Dflood protocol as employed in this study adheres to the rules listed in Fig. 9. We use protocol parameter values (as defined by Fig. 9) which by experience over time have proven to work well: $T_{\min} = 5$ s, $T_{\max} = 65$ s, $N_{\text{Dupl}} = 2.5$ s, $T_{\text{Dupl}} = 20$ s, and $T_{\text{Retrans}} = 60$ s. With respect to the maximum number of retransmissions, we investigate the different possibilities $N_{\text{Retrans}} \in \{0, 1, 2\}$.

Note that a sink-packet extension to Dflood has also been proposed [42], which can improve protocol performance in large networks. This extension is not considered in this paper.

The medium-access control (MAC) protocol is ALOHA with carrier sensing, i.e., if the modem is in the receive state, the MAC protocol will refrain from transmitting until after the modem is back in the idle state. In the network simulations, the modem is modeled to go from the idle state to the receive state when the received SNR is above an acquisition threshold parameter (to approximate the typical modem behavior of correlation with detection preamble exceeding a detection threshold). The acquisition threshold is set to a value which approximates the preamble detection shown in Fig. 8. For each of the four rates, the acquisition threshold is set to the SNR at which 50% of the packets are detected (-0.6 dB, -4.4 dB, -7.9 dB, and -11.0 dB, respectively, for $R = 1, 2, 3, 4$).

VII. LUT Approach Applied to the Case Study

The network simulation framework used in this work is described in [20]. It uses the ns2 software with the NS-MIRACLE/DESERT[3] extensions, further augmented with some RACUN-specific modules. Tapparello *et al.* [20] also describe further details of the LUT method for physical-layer modeling which plays a key role in this paper.

A. Propagation and Noise Model

The network simulator uses empirical equations for propagation loss and noise to compute the SNR of communication packets received in simulation. The underwater propagation model in DESERT combines Thorp's absorption formula [43] with spreading losses with user configurable decibel per decade. For this work, we have modified DESERT to use the absorption formula of Francois and Garrison [44] with input parameters pertinent to KAM11[4]: A temperature of 25 °C, a pH value of 8, a salinity of 35 ppt, and a depth of 50 m, which is in the middle of the water column. The resulting absorption coefficient α amounts to 0.342 dB/km at the signal center frequency of 6 kHz.

Fig. 10 shows the propagation loss (PL) calculated from the recorded KAM11 probe signals (red circles), using an estimated source level of 176.5 dB re 1 μPa^{2}m^2, which is in relatively good agreement with numerical results based on environmental modeling (blue triangles). The modeling result is a smoothed PL by an incoherent modal summation [45], appropriate for shallow-water environments where modes are bottom interacting and the detailed interference patterns are not always meaningful. However, this model is computationally demanding and we strive to approach the measured PL with a simple empirical approach. Superimposed are the spherical spreading loss (black line) and another empirical PL which uses environmental knowledge (blue line). The second approach has spherical spreading close to the source, and further assumes that boundary reflection losses set in as soon as the sound becomes trapped in the waveguide at a horizontal distance $r_1 \approx H/(2\tan\phi_c)$, where H denotes the water depth and ϕ_c is the seabed critical angle

$$\text{PL} = 20\log_{10}\frac{r}{r_0} + \alpha r \; r < r_1 \tag{6}$$

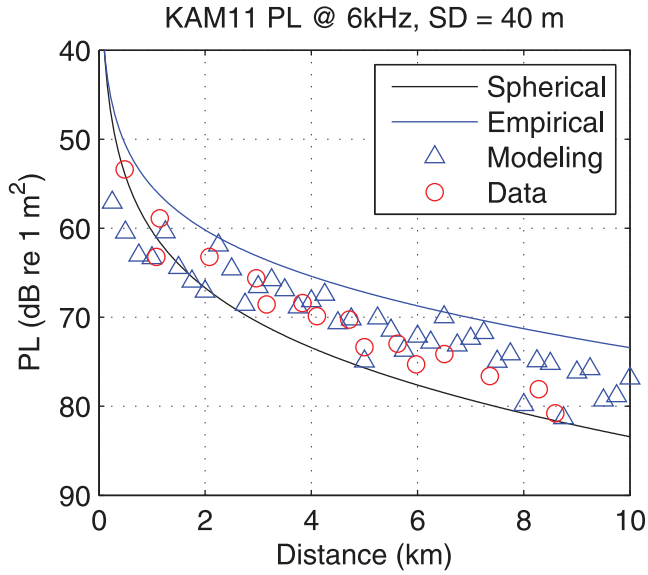

Fig. 10. Comparison of different propagation loss models with measured propagation loss in the investigated KAM11 data set.

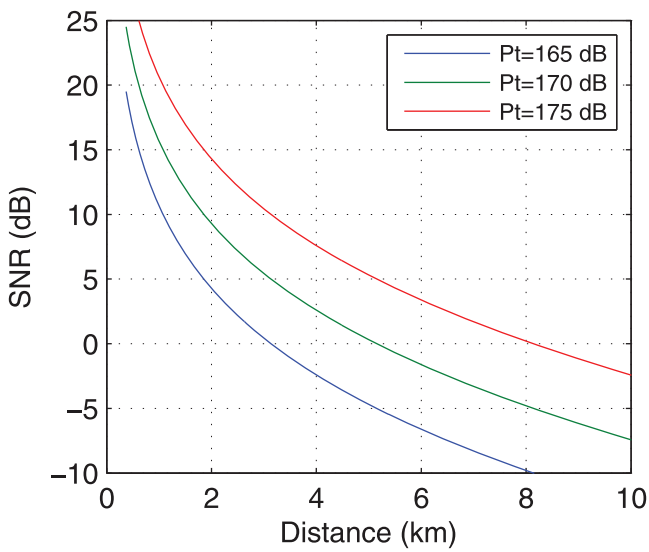

Fig. 11. Modeled SNR as a function of distance and source level P_t (in dB re 1 μPa^{2}m^2).

[3]NS-MIRACLE = Multi-InteRfAce Cross-Layer Extension library for the Network Simulator, DESERT = an NS-Miracle extension to DEsign, Simulate, Emulate and Realize Test-beds for Underwater network protocols.

[4]Francois and Garrison's formula is more accurate for the shallow KAM11 waters than Thorp's equation, which is for the deep ocean.

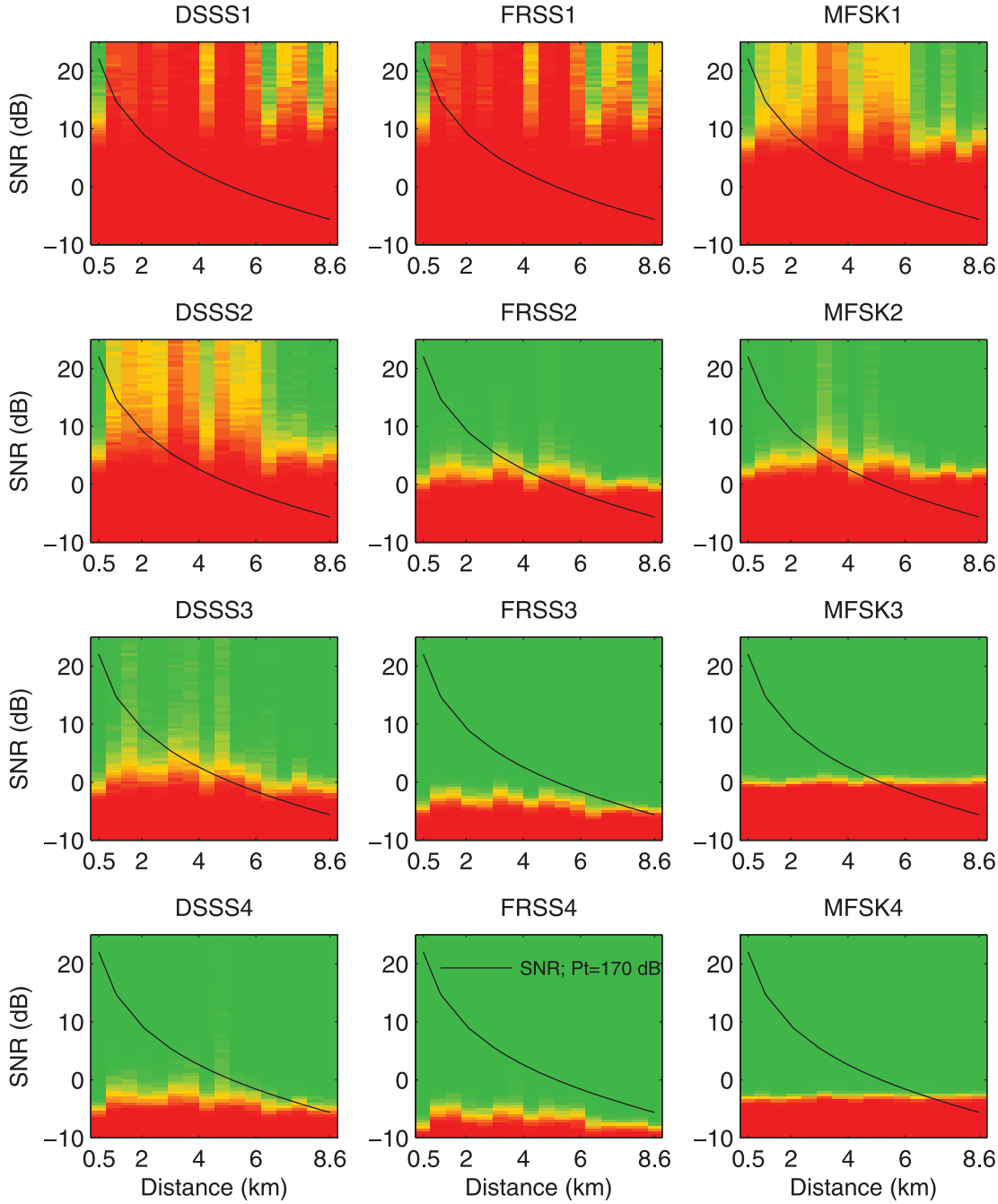

Fig. 12. LUTs generated from channel replay simulations. Color coding shows the PER, from zero (green) to one (red) using the color scale shown in Fig. 14. Superimposed is the modeled SNR versus distance at a source level of 170 dB re 1 μPa^{2}m^2.

$$= 15 \log_{10} \frac{r}{r_0} + 5 \log_{10} \frac{r_1}{r_0} + \alpha r, \qquad r \geq r_1 \qquad (7)$$

where the reference distance $r_0 = 1$ m provides PL in units of dB re 1 m^2 [2]. The value of $\phi_c = 22^\circ$ follows from KAM11 environmental data. The $15 \log_{10} r$ spreading accounts for bottom-reflection losses and is known as the "mode stripping" region [2]. The black and blue lines both include absorption loss at 6 kHz. Interestingly, the two curves provide upper and lower bounds on the measured PL, respectively. The spherical loss has a root mean square (RMS) deviation from the measured PL of 3.4 dB, and is adopted for the network simulations. Spherical spreading is the worst scenario, ensuring that the choice of PL model does not lead to overestimation of network performance. The simulation results are valid, within a source level uncertainty of a few decibels.

The noise model in DESERT uses empirical noise spectra, from [46]. For this study, the parameters of the noise model have been adjusted to give a total noise level of 94 dB re 1 μPa^2 for ACGN in the 4–8-kHz band. This is in agreement with KAM11 noise spectra [35].

B. PER Versus Distance

The SNR model from Section VII-A gives the SNR as a function of distance and source level, illustrated in Fig. 11 for three

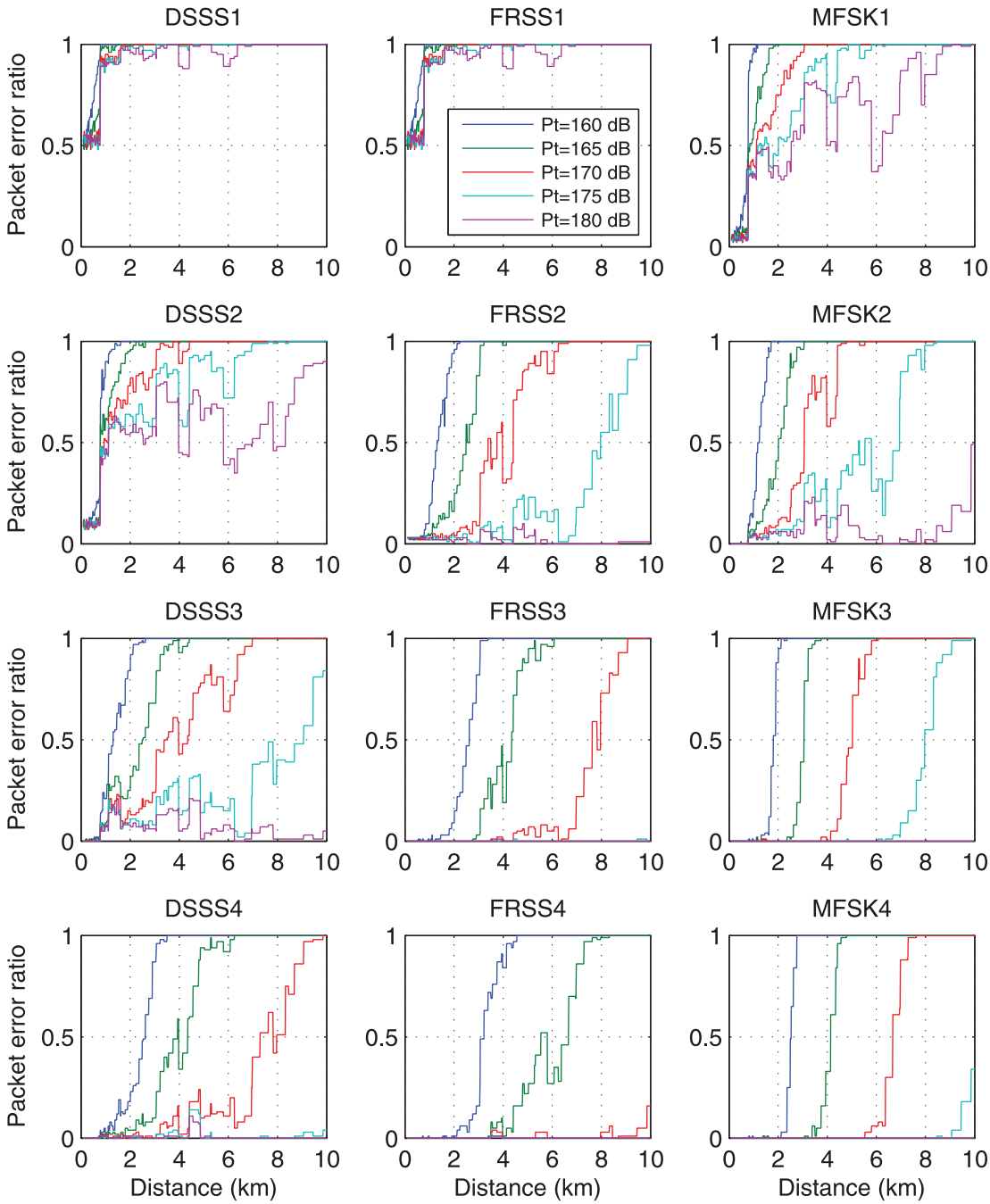

Fig. 13. Modeled PER versus distance and source level P_t (in dB re 1 μPa^{2}m^2) when using LUTs for the considered physical-layer schemes.

source levels P_t. On the other hand, the channel replay simulations give the PER as a function of distance and SNR. Fig. 12 shows these PERs on a red–green color scale.

Here, we see that the PER of MFSK3 and MFSK4 at each SNR value is virtually independent of range, thanks to the guard interval which mitigates reverberation. All other signals show variation with range, because the delay-Doppler spread varies with distance. The mode stripping illustrated by Fig. 5 renders the communication channel more benign at the longest ranges. This explains why the curves in Fig. 8, which are range averages, reveal steep transitions for MFSK3 and MFSK4 and more gradual transitions for the other signals. Fig. 12 confirms that MFSK is the best performer at the highest tested rate, and FRSS at the other rates, although the differences are range dependent.

The PER as a function of distance and SNR in Fig. 12 can be combined with Fig. 11 to give the PER as a function of distance and source level. To illustrate this, one of the curves from Fig. 11 is superimposed on each panel of Fig. 12. For a given distance, the PER is then given by the color where this curve traverses the image. Fig. 13 shows the resulting PER for all signals, as a function of distance and source level. The LUT interface of DESERT applies nearest neighbor interpolation in distance (to the nearest measurement distance) and SNR (at a LUT resolution of 0.5 dB), which explains the steps in the plots and implies

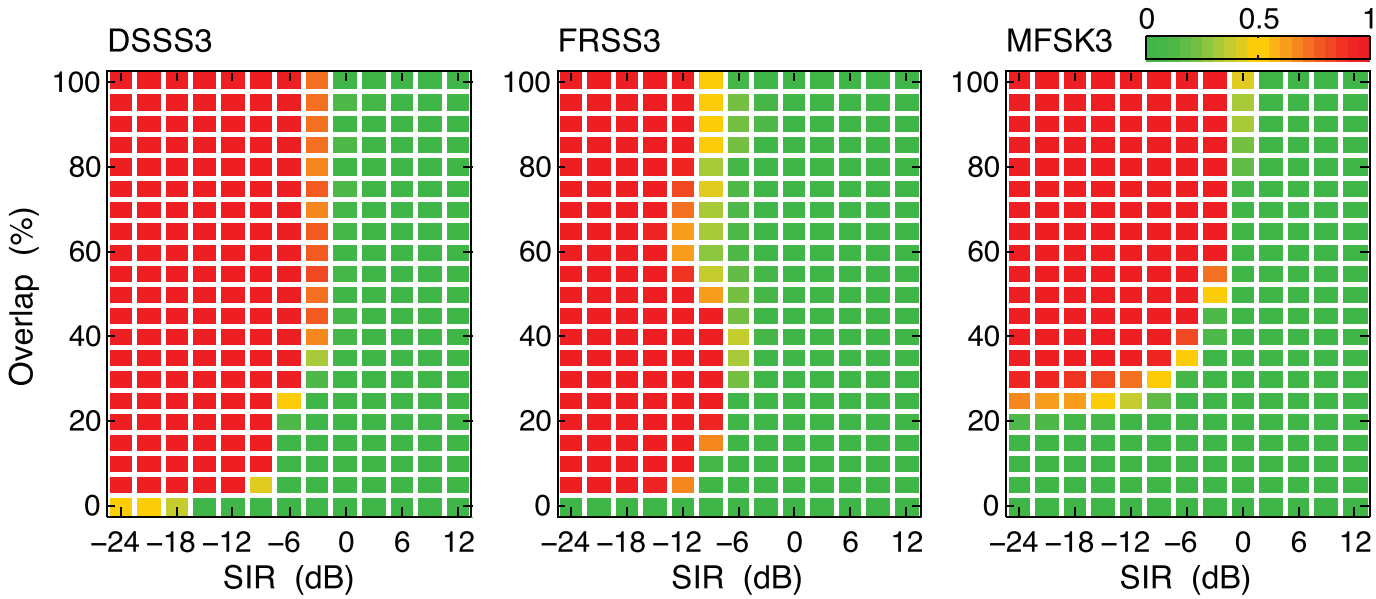

Fig. 14. Example collision LUTs. The color code gives the PER.

that above the maximum measurement distance of 8.6 km, only the SNR will make a difference.

Note from Fig. 13 that the modeled PER does not always increase monotonically with distance. This is a realistic feature, which arises because the delay-Doppler spread does not vary with the range in a simple way, and which is not captured by a model based on SNR alone.

C. Modeling of Collisions

In networks with busy traffic, it is important for the network simulator to have some knowledge of packet errors due to collisions. Such knowledge is available in the form of collision LUTs. To create the collision LUTs, signals of the same type, but carrying different random bit streams, were fed to the receivers with various degrees of overlap and interference strength. Delay-Doppler spreading was not included, but simple Doppler shifts were applied to packets to get more statistical variation. Fig. 14 illustrates the resulting collision LUTs for DSSS3, FRSS3, and MFSK3. The graphs show the PER for the first of two received packets versus the degree of overlap and the signal-to-interference ratio (SIR).

MFSK3 tolerates stronger interference up to ≈20% overlap. One reason is that the wideband detection preamble of the interfering packet does less harm to the FSK tones than to the wideband FRSS and DSSS waveforms. On the other hand, FRSS can tolerate stronger interference at large overlaps, for the same reason that it has the best performance at low SNR (see Section V-C).

In the network simulations, it is assumed that the receiver in case of collisions will only try to demodulate the first received packet (with SNR above the acquisition threshold), i.e., it is not searching for other detection preambles while receiving the packet corresponding to one acquired detection preamble. The handling of collisions in NS-MIRACLE/DESERT is further detailed in [20].

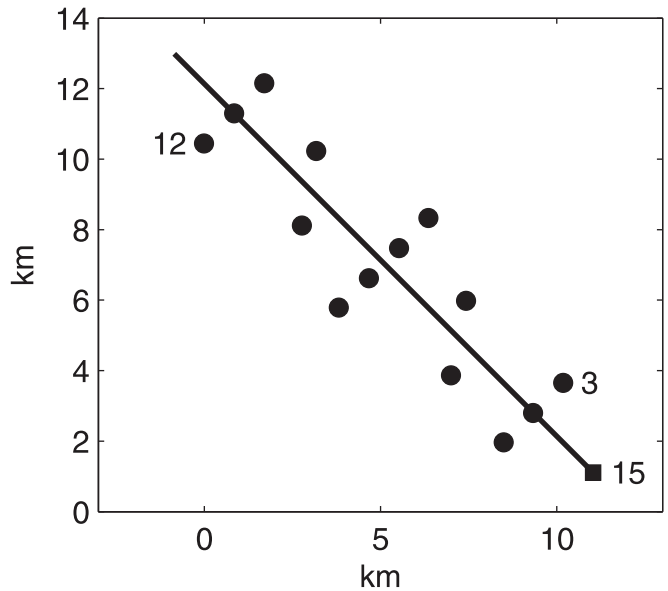

Fig. 15. Simulated network layout. The circular markers are bottom nodes, the line segment shows the AUV trajectory, and the square marker shows the AUV starting position. Source and sink nodes are marked by numbers (the AUV is node number 15).

D. Shortcomings of the Proposed Approach

We are of the opinion that the proposed approach is among the most realistic means presently available for simulation of underwater communication networks. The LUTs are built using a validated channel replay physical-layer simulator, which offers high realism but requires measurements of the time-varying impulse response at a variety of source–receiver distances in the environment to be simulated. Also, the applied propagation loss and noise models are validated against measurements in the same environment. Still, some shortcomings remain.

One obvious shortcoming is that it is only possible to simulate environments in which a suitable channel measurement campaign has been performed. And even with a relatively densely

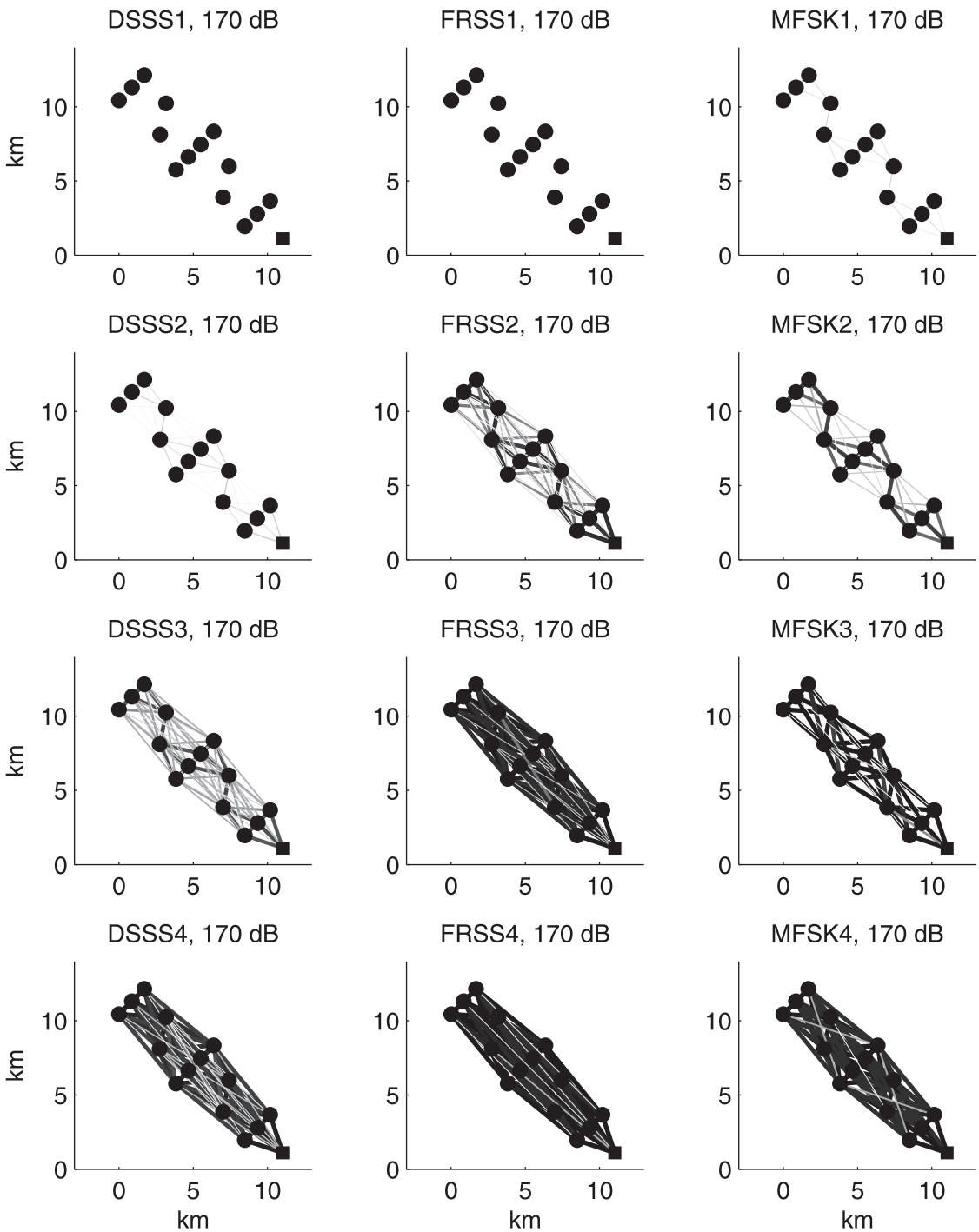

Fig. 16. Connectivity map for the different physical layers at a source level of 170 dB re 1 μPa^{2}m^2, with the AUV in its starting position (bottom right). The thickness and darkness of each edge are proportional to $(1 - \mathrm{PER})$. In cases of overlapping edges, thin and light edges are plotted on top of thick and dark edges.

sampled data set, as the one used here, the nearest neighbor interpolation adds uncertainties. Other shortcomings are assumptions that may be nonrealistic. First, channel conditions are assumed to be a function of distance alone, while in reality there may be variations over depth, bearing, and time as well. Second, all links are assumed to be reciprocal. In reality, nonreciprocal links may result, for example, from different local noise levels at different nodes, or from different receive and transmit transducer characteristics. Differences in noise level and hardware characteristics should be straightforward to implement in the network simulation setup, when the effects are fully understood. Modeling and implementing variations in channel conditions over space and time would be a far more comprehensive task.

Unfortunately, the network simulation method is not yet validated. Such validation would require a sea trial with extensive testing of a multinode underwater acoustic network, and simultaneous measurement of the time-varying impulse response at a variety of distances. These are two resource demanding tasks.

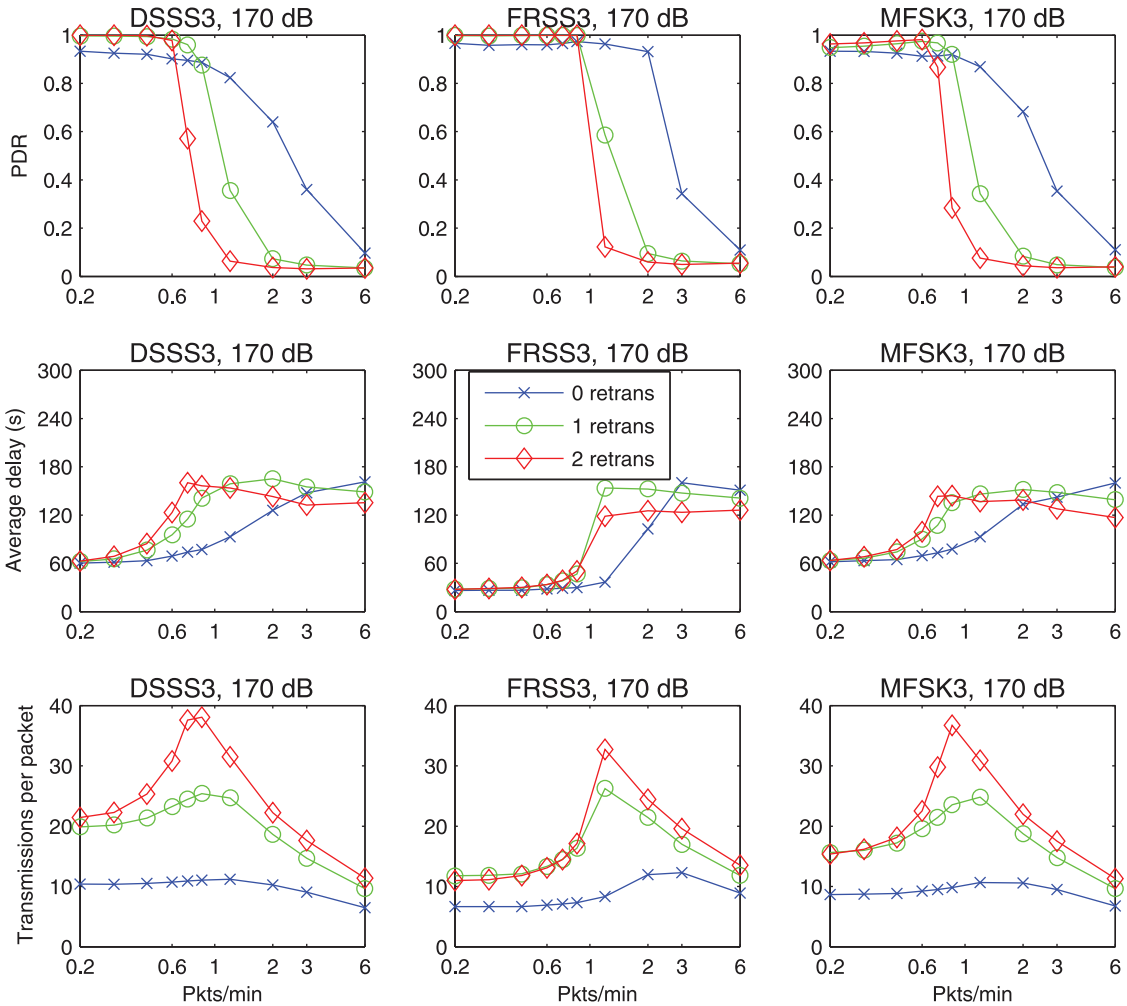

Fig. 17. Network simulation results using the $R = 3$ physical-layer waveforms at a source level of 170 dB re 1 μPa^{2}m^2. The abscissa shows the packet generation rate at each of the two source nodes.

VIII. Network Simulations

A. Simulated Network Layout and Traffic Pattern

Fig. 15 shows the simulated network layout. The scenario is inspired by, but not identical to, a simulation scenario defined and used inside the RACUN project. Ten bottom nodes are arranged on three straight lines 6 km apart, with 1.2-km internode separation on each line. Four additional bottom nodes are placed as repeaters in the areas between the lines, making it possible to connect the network if the physical layer can support a link distance of 2.4 km. Node 15 is an autonomous underwater vehicle (AUV) which moves back and forth at 2.06 m/s (4 kn) along the plotted line segment.

There are two source nodes and two sink (destination) nodes in the network. Traffic is sent unicast from node 15 to node 3 in the lower right corner, and multicast from node 12 in the upper left corner to node 15 and node 3. The two sources generate their messages simultaneously (to stress the network), at a regular interval which is adjusted to investigate the network performance as a function of traffic load. Each message is 256 b, including network protocol header, matching the investigated physical-layer methods.

For each parameter combination, simulation results are averaged over 30 runs. In each of these simulation runs, 300 packets have been sent from each of the two sources. Each presented data point is hence averaged over 18 000 packets sent into the simulated network from the sources.

B. Connectivity Maps

When interpreting network simulation results, it is instructive to have a picture of the connectivity in the network under the applied physical-layer model. This can be visualized by connectivity maps, as shown in Fig. 16 for a source level of 170 dB re 1 μPa^{2}m^2. Each edge between two nodes represents the PER from Fig. 13 corresponding to the distance between the two nodes. Here, we see that the topology of the network varies from almost fully connected (for FRSS4) to fully disconnected (for FRSS1 and DSSS1).

IX. Simulation Results

In this study, network simulations are performed with the objective of assessing the impact on network performance of the following parameters:

- choice of physical layer and data rate;
- transmit source level;
- maximum number of retransmissions.

First, we present a focused study comparing the three modulation schemes and a different number of retransmissions at a

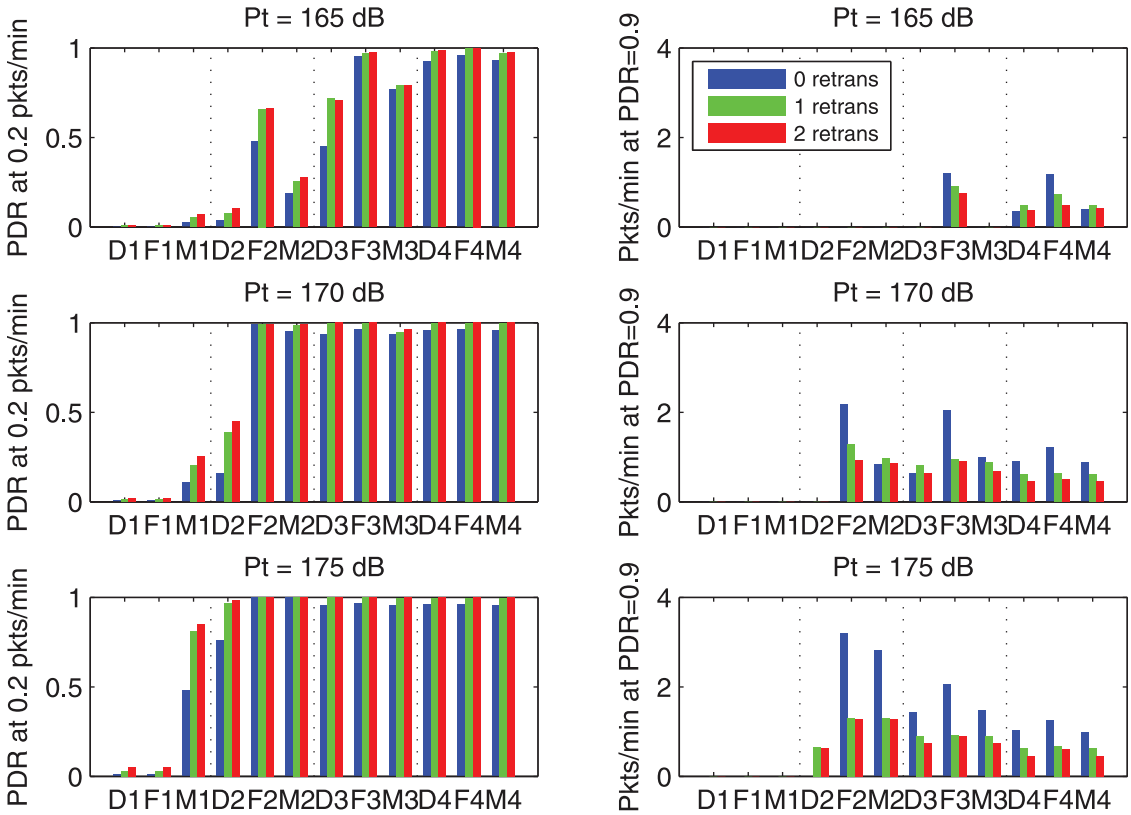

Fig. 18. Network performance as a function of the modulation scheme (D = DSSS, F = FRSS, M = MFSK), data rate, source level P_t (in dB re 1 μPa^{2}m^2), and a maximum number of retransmissions.

single combination of data rate and source level. Then, we investigate how key performance parameters vary with modulation type, data rate, and source level across a larger parameter space.

It should be stressed that only a single network topology and a single environment are considered here, so exact results cannot be generalized. However, the results serve to illustrate some typical tradeoffs in underwater networks.

A. Detailed Study at One Data Rate and Source Level

Fig. 17 shows the simulated network performance when using the $R = 3$ physical-layer waveforms at a source level of 170 dB re 1 μPa^{2}m^2. As seen in Fig. 16, the connectivity in the simulated network is quite different between DSSS3, FRSS3, and MFSK3 at this source level: FRSS3 gives a well-connected network, where relatively good paths of maximum two hops are present between all pairs of nodes in the network. DSSS3 gives a network that is equally connected in terms of possible paths through the network, but where the links have lower and more varying quality than with FRSS3. MFSK3, on the other hand, gives a network with less connectivity (four hops are required to get from one end to the other) but where the links that are present mostly are good.

The upper row of plots in Fig. 17 shows the packet delivery ratio (PDR), not to be confused with (1−PER) where PER as defined earlier in this paper is the PER for individual links. The PDR is here defined through the network, as the number of packets received at the sinks divided by the number of packets that should have been received at the sinks. Only packets successfully received with a source-to-sink delay less than 300 s are counted, due to an operational requirement in the RACUN project to deliver packets within 5 min. We see that without retransmissions, the PDR at low traffic level is in the range 0.90–0.95. At low traffic level, allowing one retransmission increases the PDR, quite significantly considering that the deviation of PDR from 1.00 is a measure of the robustness of the communication system. But in this scenario a second retransmission does not yield much further improvement. On the other hand, retransmissions lower the performance at high traffic loads due to the increased number of collisions, while without retransmissions the degradation as traffic increases is more graceful.

Allowing one retransmission gives a PDR close to one with FRSS3 at low traffic load. Surprisingly, DSSS3 achieves the same PDR, whereas MFSK3 remains behind. In all likelihood, this is due to the lower connectivity of the MFSK3 network. Fig. 16 shows that DSSS3 has links over longer ranges. Also note the dip in the DSSS3 PER at around 6 km (the distance between the three main lines of nodes) in Fig. 13, which is absent for MFSK3. Although all MFSK3 links are stronger (but not perfect, contrary to what could be deduced from Fig. 13, because collisions also play a part) than the corresponding DSSS3 links, the latter scheme has more possible paths through the network which the combination of flooding and retransmissions can exploit.

The center row of plots in Fig. 17 shows the average delay from source to sink, averaged only over packets successfully received within the 300-s delay constraint. With the protocol parameters applied here, an average delay of about 30 s corresponds to most packets reaching the sink in two hops without retransmissions. We see that this is the case with FRSS3 at low

traffic loads, but not with DSSS3 and MFSK3 where more hops are generally required. As traffic in the network increases toward saturation, the average delay increases because collisions will start hindering the first chances to get a message through.

The bottom row of plots in Fig. 17 shows the total number of packets transmitted by all nodes in the network (including forwardings, retransmissions, and receive notification packets), divided by the total number of packets generated by the two sources. Recall that one source generates unicast packets and the other source generates multicast packets. A successfully received unicast packet will lead to at least two transmissions in the network (the original transmission from the source, plus the "receive notification" for last-hop acknowledgment from the sink), whereas the multicast packets may be flooded by all 15 nodes since last-hop acknowledgment is disabled for multicast packets. Therefore, it makes sense that the value of this metric in the well-connected FRSS3 network at low traffic loads, with retransmissions disabled, is below $(2 + 15)/2 = 8.5$.

As the traffic load put into the network from the source nodes increases, we see that the relative number of transmissions in the network also increases, again because collisions start hindering the first chances to get a message through. This increased number of transmissions per packet will cause even more collisions, up to a point where the network is completely saturated and the curves start to drop off again because not all packets reach all nodes. The maximum possible number of transmissions per packet is $N_{\mathrm{Nodes}} \times (N_{\mathrm{Retrans}} + 1)$, where N_{Nodes} is the total number of nodes (15 in the simulated network) and N_{Retrans} is the maximum number of retransmissions.

B. Comparison of Different Rates and Source Levels

The plots of PDR versus traffic load in Fig. 17 (upper row) have a generic shape from which we can extract two key performance parameters: the PDR at low traffic load (here, 0.2 packets/min), and the traffic load at which the PDR crosses a certain threshold. These two performance parameters, using a PDR threshold of 0.9, are presented in Fig. 18 as a function of a modulation scheme, data rate, and source level. The point where the curves cross the PDR $= 0.9$ threshold is approximated by linear interpolation on a linear scale between simulated data points.

The general message from this figure is again as follows:

- allowing retransmissions increases the PDR at low traffic, especially for the high data rates;
- in many cases, one retransmission is sufficient to achieve a PDR close to 1;
- allowing retransmissions decreases the amount of traffic that can be supported by the network (owing to collisions).

A few exceptions can be seen from the latter observation. When retransmissions increase the PDR at low or moderate traffic load from below 0.9 to above 0.9, the amount of traffic that can be supported by the network according to the PDR$\geq$0.9 criterion increases. One example is DSSS4 at a source level of 165 dB re 1 μPa^{2}m^2, as can be seen from Fig. 19 where the PDR $= 0.9$ threshold is superimposed on the curves showing PDR versus traffic load.

Another observation from Fig. 18 is that if the physical-layer data rate can be chosen, one should choose the highest data rate that will give a reasonably well-connected network. As expected, this rate increases with the source level. One example is FRSS at a source level of 170 dB re 1 μPa^{2}m^2, where FRSS2 gives a higher PDR at low traffic loads and zero retransmissions, as well as support for higher traffic load, compared to FRSS3 and FRSS4.The reason is fewer collisions, because of the shorter packet duration and because of the shorter interference distance due to the higher acquisition threshold. As seen in Fig. 16, FRSS2 gives a network that is well connected, but each node will have fewer one-hop neighbors (potential interferers) than with FRSS3 or FRSS4.

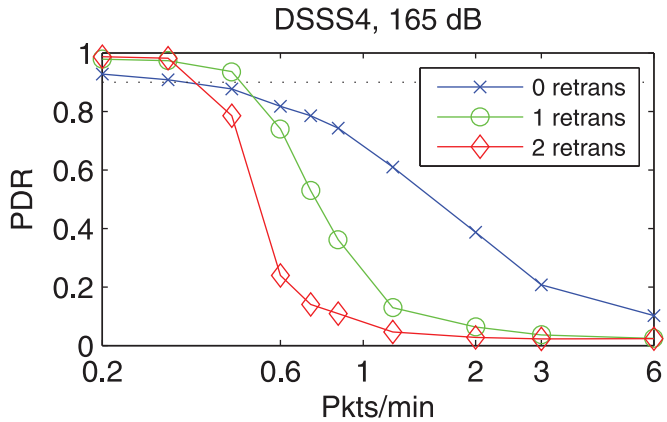

Fig. 19. Network simulation results using the DSSS4 at a source level of 165 dB re 1 μPa^{2}m^2. The abscissa shows the packet generation rate at each of the two source nodes. A dotted line is drawn at PDR $= 0.9$.

X. Conclusion

Network simulations were performed with link-layer statistics obtained from channel replay simulations. In spite of some shortcomings (see Section VII-D), we are of the opinion that the proposed approach is among the most realistic means presently available for simulation of underwater communication networks. The LUTs are built with a validated physical-layer simulator, and the applied SNR model was validated to within a few decibels against measurements in the same environment.

The physical-layer simulations confirm that there can be a big gap between the textbook performance of modulation schemes and their performance in acoustic channels, where a high SNR does not guarantee low error rates. There are also sizable differences between the compared schemes. These differences are due to the different modulation formats as well as implementation choices and parameter settings.

The network simulation results demonstrate how retransmissions in a reduced flooding protocol pose a tradeoff between performance at high and low traffic loads. It is also demonstrated that if the physical-layer data rate can be chosen, for a given PSDU size, the best network performance is achieved if one chooses the highest data rate that yields a reasonably well-connected network. A high rate yields a short signal length and mitigates collisions. Collision avoidance is more important than the extended connectivity offered by low-rate signaling in the considered scenarios. By contrast, at a given bit rate, a physical layer with extended connectivity but relatively weak links may be preferred to one with stronger links over fewer connections.

ACKNOWLEDGMENT

The authors would like to thank partners of the EDA project RACUN [27] for the joint development of the presented network simulation method. In particular, they would like to thank Consorzio Ferrara Ricerche (CFR) for the NS-MIRACLE and DESERT additions to ns2, and the late G. Toso of CFR for implementing the LUT interface to DESERT. They also thank H. Austad for the initial implementation of the retransmission scheme for Dflood in his M.Sc. work. The KAM11 experiment was sponsored by the U.S. Office of Naval Research, Code 322OA, with support from the *R/V Kilo Moana* and the Pacific Missile Range Facility.

REFERENCES

[1] D. E. Weston, "Intensity-range relations in oceanographic acoustics," *J. Sound Vib.*, vol. 18, no. 2, pp. 271–287, 1971.

[2] M. Ainslie, P. Dahl, C. de Jong, and R. Laws, "Practical spreading laws: The snakes and ladders of shallow water acoustics," in *Proc. 2nd Int. Conf. Exhibit. Underwater Acoust.*, Rhodes, Greece, Jun. 22–27, 2014.

[3] C. Kam, S. Kompella, G. D. Nguyen, A. Ephremides, and J. Zaihan, "Frequency selection and relay placement for energy efficiency in underwater acoustic networks," *IEEE J. Ocean. Eng.*, vol. 39, no. 2, pp. 331–342, Apr. 2014.

[4] Y. Noh *et al.*, "DOTS: A propagation delay-aware opportunistic MAC protocol for mobile underwater networks," *IEEE Trans. Mobile Comput.*, vol. 13, no. 4, pp. 766–782, Apr. 2014.

[5] S. Azad, P. Casari, and M. Zorzi, "The underwater selective repeat error control protocol for multiuser acoustic networks: Design and parameter optimization," *IEEE Trans. Wireless Commun.*, vol. 12, no. 10, pp. 4866–4877, Oct. 2013.

[6] D. B. Kilfoyle and A. B. Baggeroer, "The state of the art in underwater acoustic telemetry," *IEEE J. Ocean. Eng.*, vol. 25, no. 1, pp. 4–27, Jan. 2000.

[7] R. Otnes, P. A. van Walree, and T. Jenserud, "Validation of replay-based underwater acoustic communication channel simulation," *IEEE J. Ocean. Eng.*, vol. 38, no. 4, pp. 689–700, Oct. 2013.

[8] R. Otnes, P. A. van Walree, and T. Jenserud, "Erratum to "Validation of replay-based underwater acoustic communication channel simulation"," *IEEE J. Ocean. Eng.*, vol. 38, no. 4, p. 809, Oct. 2013.

[9] J. Preisig, "Acoustic propagation considerations for underwater acoustic communications network development," *ACM SIGMOBILE Mobile Comput. Commun. Rev.*, vol. 11, no. 4, pp. 2–10, Oct. 2007.

[10] P. A. van Walree, "Propagation and scattering effects in underwater acoustic communication channels," *IEEE J. Ocean. Eng.*, vol. 38, no. 4, pp. 614–631, Oct. 2013.

[11] T. Jenserud and R. Otnes, "Reverberation tail in power delay profiles: Effects and modeling," in *Proc. MTS/IEEE OCEANS Conf.*, Bergen, Norway, Jun. 2013, DOI: 10.1109/OCEANS-Bergen.2013.6608063.

[12] J. C. Preisig and G. B. Deane, "Surface wave focusing and acoustic communications in the surf zone," *J. Acoust. Soc. Amer.*, vol. 116, no. 4, pp. 2067–2080, Oct. 2004.

[13] A. Song *et al.*, "Passive time reversal acoustic communications through shallow-water internal waves," *IEEE J. Ocean. Eng.*, vol. 35, no. 4, pp. 756–765, Oct. 2010.

[14] M. Siderius, M. B. Porter, P. Hursky, and V. McDonald, "Effects of ocean thermocline variability on noncoherent underwater acoustic communications," *J. Acoust. Soc. Amer.*, vol. 121, no. 4, pp. 1895–1908, Apr. 2007.

[15] N. Parrish, L. Tracy, S. Roy, P. Arabshahi, and W. L. J. Fox, "System design considerations for undersea networks: Link and multiple access protocols," *IEEE J. Sel. Areas Commun.*, vol. 26, no. 9, pp. 1720–1730, Dec. 2008.

[16] P. Qarabaqi and M. Stojanovic, "Statistical characterization and computationally efficient modeling of a class of underwater acoustic communication channels," *IEEE J. Ocean. Eng.*, vol. 38, no. 4, pp. 701–717, Oct. 2013.

[17] P. A. van Walree, T. Jenserud, and M. Smedsrud, "A discrete-time channel simulator driven by measured scattering functions," *IEEE J. Sel. Areas Commun.*, vol. 26, no. 9, pp. 1628–1637, Dec. 2008.

[18] F.-X. Socheleau, C. Laot, and J.-M. Passerieux, "Stochastic replay of non-WSSUS underwater acoustic communication channels recorded at sea," *IEEE Trans. Signal Process.*, vol. 59, no. 10, pp. 4838–4849, Oct. 2011.

[19] Y. Isukapalli, H. Song, and W. Hodgkiss, "Stochastic channel simulator based on local scattering function," *J. Acoust. Soc. Amer.*, vol. 130, pp. EL200–EL205, 2011.

[20] C. Tapparello *et al.*, "Performance evaluation of forwarding protocols for the RACUN network," in *Proc. 8th ACM Int. Conf. Underwater Netw. Syst. (WuWNet)*, Kaohsiung, Taiwan, Nov. 2013, Art. no. 36.

[21] R. Otnes, P. van Walree, and H. Song, "Network simulation with lookup tables from physical layer replay simulations: A KAM11 example," in *Proc. Underwater Commun. Netw. Conf.*, Sestri Levante, Italy, Sep. 2014, DOI: 10.1109/UComms.2014.7017147.

[22] F. Guerra, P. Casari, and M. Zorzi, "World ocean simulation system (WOSS): A simulation tool for underwater networks with realistic propagation modeling," in *Proc. 4th ACM Int. Workshop UnderWater Netw. (WuWNet)*, Berkeley, CA, USA, Nov. 2009, Art. no. 4.

[23] P. Casari *et al.*, "Open source suites for underwater networking: WOSS and DESERT underwater," *IEEE Network*, vol. 28, no. 5, pp. 38–46, Sep./Oct. 2014.

[24] B. Tomasi *et al.*, "On modeling JANUS packet errors over a shallow water acoustic channel using Markov and hidden Markov models," in *Proc. IEEE Military Commun. Conf.*, San Jose, CA, USA, Oct. 2010, pp. 2406–2411.

[25] B. Tomasi, G. Toso, P. Casari, and M. Zorzi, "Impact of time-varying underwater acoustic channels on the performance of routing protocols," *IEEE J. Ocean. Eng.*, vol. 38, no. 4, pp. 772–784, Oct. 2013.

[26] M. Chitre, K. Pelekanakis, and M. Legg, "Statistical bit error trace modeling of acoustic communication links using decision feedback equalization," *IEEE J. Ocean. Eng.*, vol. 38, no. 4, pp. 785–795, Oct. 2013.

[27] J. Kalwa, "The RACUN-project: Robust acoustic communications in underwater networks—An overview," in *Proc. MTS/IEEE OCEANS Conf.*, Santander, Spain, Jun. 2011, DOI: 10.1109/Oceans-Spain.2011.6003495.

[28] P. van Walree, H. Buen, and R. Otnes, "A performance comparison between DSSS, M-FSK, and frequency-division multiplexing in underwater acoustic channels," in *Proc. Underwater Commun. Netw. Conf.*, Sestri Levante, Italy, Sep. 2014, DOI: 10.1109/UComms.2014.7017133.

[29] M. Stojanovic and L. Freitag, "Multichannel detection for wideband underwater acoustic CDMA communications," *IEEE J. Ocean. Eng.*, vol. 31, no. 3, pp. 685–695, Jul. 2006.

[30] M. Stojanovic, J. A. Catipovic, and J. G. Proakis, "Phase-coherent digital communications for underwater acoustic channels," *IEEE J. Ocean. Eng.*, vol. 19, no. 1, pp. 100–111, Jan. 1994.

[31] P. A. van Walree and G. Leus, "Robust underwater telemetry with adaptive turbo multiband equalization," *IEEE J. Ocean. Eng.*, vol. 34, no. 4, pp. 645–655, Oct. 2009.

[32] J. G. Proakis and M. Salehi, *Digital Communications*, 5th ed. New York, NY, USA: McGraw-Hill, 2008, p. 656.

[33] K. F. Scussel, J. A. Rice, and S. Merriam, "A new MFSK acoustic modem for operation in adverse underwater channels," in *Proc. MTS/IEEE OCEANS Conf.*, Halifax, NS, Canada, Oct. 1997, pp. 247–254.

[34] W. S. Hodgkiss and J. C. Preisig, "Kauai ACOMMS MURI 2011 (KAM11) experiment," in *Proc. Eur. Conf. Underwater Acoust.*, Edinburgh, U.K., Jul. 2012, pp. 993–1000.

[35] H. C. Song and W. S. Hodgkiss, "Efficient use of bandwidth for underwater acoustic communication," *J. Acoust. Soc. Amer.*, vol. 134, pp. 905–908, 2013.

[36] Y. Choo, W. Seong, and H. Song, "Emergence of striation patterns in acoustic signals reflected from dynamic surface waves," *J. Acoust. Soc. Amer.*, vol. 136, no. 3, pp. 1046–1053, 2014.

[37] G. Matz, A. F. Molisch, F. Hlawatsch, M. Steinbauer, and I. Gaspard, "On the systematic measurement errors of correlative mobile radio channel sounders," *IEEE Trans. Commun.*, vol. 50, no. 5, pp. 808–821, May 2002.

[38] B. Sklar, *Digital Communications*. Englewood Cliffs, NJ, USA: Prentice-Hall, 2001, p. 212.

[39] R. Otnes and S. Haavik, "Duplicate reduction with adaptive backoff for a flooding-based underwater network protocol," in *Proc. MTS/IEEE OCEANS Conf.*, Bergen, Norway, Jun. 2013, DOI: 10.1109/OCEANS-Bergen.2013.6608038.

[40] H. Austad, "Simulation of subsea communication network," M.S. thesis, Dept. Inf., Univ. Oslo, Oslo, Norway, May 2014.

[41] S.-Y. Ni, Y.-C. Tseng, Y.-S. Chen, and J.-P. Sheu, "The broadcast storm problem in a mobile ad hoc network," in *Proc. 5th Annu. ACM/IEEE Int. Conf. Mobile Comput. Netw.*, Seattle, WA, USA, Aug. 2009, pp. 151–162.
[42] A. Komulainen and J. Nilsson, "Capacity improvements for reduced flooding using distance to sink information in underwater networks," in *Proc. Underwater Commun. Netw. Conf.*, Sestri Levante, Italy, Sep. 2014, DOI: 10.1109/UComms.2014.7017149.
[43] W. H. Thorp, "Analytic description of the low-frequency absorption coefficient," *J. Acoust. Soc. Amer.*, vol. 42, p. 270, 1967.
[44] R. E. Francois and G. R. Garrison, "Sound absorption based on ocean measurements. Part II: Boric acid contribution and equation for total absorption," *J. Acoust. Soc. Amer.*, vol. 72, no. 6, pp. 1879–1890, Dec. 1982.
[45] F. Jensen, W. Kuperman, M. Porter, and H. Schmidt, *Computational Ocean Acoustics*. New York, NY, USA: Springer-Verlag, 2011, ch. 5.2.
[46] R. Urick, *Principles of Underwater Sound*, 3rd ed. New York, NY, USA: McGraw-Hill, 1983, p. 210.

Roald Otnes (S'00–M'03–SM'13) received the M.Sc. and Ph.D. degrees in telecommunications from the Norwegian University of Science and Technology, Trondheim, Norway, in 1998 and 2003, respectively.

Since 2003, he has been a Scientist at the Norwegian Defence Research Establishment (FFI), Horten, Norway. His current research interests include underwater acoustic communications and sonar signal processing.

Paul A. van Walree (M'08) received the M.Sc. and Ph.D. degrees in solid-state physics from Utrecht University, Utrecht, The Netherlands, in 1992 and 1997, respectively.

From 1998 to 2009, he was an Underwater Acoustician at The Netherlands Organisation for Applied Scientific Research (TNO), Delft, The Netherlands. In 2009, he started as a Scientist with the Maritime Systems Department, Norwegian Defence Research Establishment (FFI), Horten, Norway. His research interests include digital underwater communications, channel characterization and simulation, and acoustic signal processing.

Helge Buen received the B.Sc. degree in electrical engineering from Vestfold University College, Horten, Norway, in 2008.

He is currently with the Norwegian Defence Research Establishment (FFI), Horten, Norway. His research interests include underwater instrumentation systems, underwater communications, and signal processing.

Heechun Song received the Ph.D. degree in ocean engineering from the Massachusetts Institute of Technology (MIT), Cambridge, MA, USA, in 1990.

From 1991 to 1995, he was with the Korea Ocean Research and Development Institute (KORDI), Ansan, Korea. Since 1996, he has been a Research Scientist in the Marine Physical Laboratory/Scripps Institution of Oceanography (MPL/SIO), University of California San Diego (UCSD), La Jolla, CA, USA. His research interests include time-reversed acoustics, waveguide physics, sonar array processing, and underwater acoustic communications.

Dr. Song is a Fellow of the Acoustical Society of America and an Associate Editor for the *Journal of Acoustical Society of America*.